

## Research Paper

# Core-shell metal-organic frameworks with fluorescence switch to trigger an enhanced photodynamic therapy

Yuan Liu<sup>1</sup>, Christina S. Gong<sup>1</sup>, Lisen Lin<sup>1</sup>, Zijian Zhou<sup>1</sup>, Yijing Liu<sup>1</sup>, Zhen Yang<sup>1</sup>, Zheyu Shen<sup>1</sup>, Guocan Yu<sup>1</sup>, Zhantong Wang<sup>1</sup>, Sheng Wang<sup>1</sup>, Ying Ma<sup>1</sup>, Wenpei Fan<sup>1</sup>, Liangcan He<sup>1</sup>, Gang Niu<sup>1</sup>, Yunlu Dai<sup>2</sup>✉, Xiaoyuan Chen<sup>1</sup>✉

1. Laboratory of Molecular Imaging and Nanomedicine, National Institute of Biomedical Imaging and Bioengineering, National Institutes of Health, Bethesda, Maryland 20892, United States
2. Faculty of Health Sciences, University of Macau, Macau, SAR 999078, P. R. China.

✉ Corresponding authors: E-mail: yldai@umac.mo; E-mail: shawn.chen@nih.gov

© Ivyspring International Publisher. This is an open access article distributed under the terms of the Creative Commons Attribution (CC BY-NC) license (<https://creativecommons.org/licenses/by-nc/4.0/>). See <http://ivyspring.com/terms> for full terms and conditions.

Received: 2019.03.09; Accepted: 2019.03.11; Published: 2019.04.13

## Abstract

The design of hybrid metal-organic framework (MOF) nanomaterials by integrating inorganic nanoparticle into MOF (NP@MOF) has demonstrated outstanding potential for obtaining enhanced, collective, and extended novel physiochemical properties. However, the reverse structure of MOF-integrated inorganic nanoparticle (MOF@NP) with multifunction has rarely been reported.

**Methods:** We developed a facile in-situ growth method to integrate MOF nanoparticle into inorganic nanomaterial and designed a fluorescence switch to trigger enhanced photodynamic therapy. The influence of “switch” on the photodynamic activity was studied *in vitro*. The *in vivo* mice with tumor model was applied to evaluate the “switch”-triggered enhanced photodynamic therapy efficacy.

**Results:** A core-satellites structure with fluorescence off and on function was obtained when growing MnO<sub>2</sub> on the surface of fluorescent zeolitic imidazolate framework (ZIF-8) nanoparticles. Furthermore, A core-shell structure with photodynamic activity off and on function was achieved by growing MnO<sub>2</sub> on the surface of porphyrinic ZrMOF nanoparticles (ZrMOF@MnO<sub>2</sub>). Both the fluorescence and photodynamic activities can be turned off by MnO<sub>2</sub> and turned on by GSH. The GSH-responsive activation of photodynamic activity of ZrMOF@MnO<sub>2</sub> significantly depleted the intracellular GSH via a MnO<sub>2</sub> reduction reaction, thus triggering an enhanced photodynamic therapy efficacy. Finally, the GSH-reduced Mn<sup>2+</sup> provided a platform for magnetic resonance imaging-guided tumor therapy.

**Conclusion:** This work highlights the impact of inorganic nanomaterial on the MOF properties and provides insight to the rational design of multifunctional MOF-inorganic nanomaterial complexes.

Key words: Metal-organic frameworks, Core-shell structure, Fluorescence switch, Photodynamic therapy

## Introduction

Photodynamic therapy, which takes advantage of photons to generate therapeutic reactive oxygen species, has emerged as an alternative to traditional surgery, chemotherapy, and radiotherapy to combat cancer [1, 2]. As a non-invasive treatment, photodynamic therapy causes fewer harmful side-effects than the conventional treatments [3].

Nanotechnology has demonstrated potential biomedical applications by combining nanomaterials and photosensitizers for collective delivery, imaging, and photodynamic therapy [4-6]. With functional nanomaterials, multi-purpose platforms, including synergistic and cascaded cancer therapy, have been achieved [7, 8].

Metal-organic framework (MOF), an emerging type of crystalline material formed by coordinating metal ions and organic linkers, has attracted significant attention because of their porous structures and unique properties at the nanometer scale [9-11]. In particular, MOF nanoparticles have shown great potential in biomedical applications owing to their uniform and well-defined structures [12-14]. Porous structure made MOF an ideal candidate as a delivery platform for disease treatment [15-18]. The preparation of nanoscale porphyrinic MOF nanoparticles solved many issues associated with porphyrinic photosensitizers, such as aggregation, self-quenching, and uncontrollable in vivo administration for cancer therapy [3, 19]. However, intracellular glutathione (GSH) is fatal to the reactive oxygen species generated from photosensitizers, especially in tumor cells which have much higher concentration of GSH than normal cells [20-23]. So, it would be ideal to develop photosensitizer-based MOF with GSH depletion function.

Recently, the design of multifunctional MOF nanomaterials by integrating inorganic nanoparticle into MOF (NP@MOF) has opened new paths to obtain enhanced, collective, and extended novel physicochemical properties [24-27]. For example, efficient and selective hydrogenation has been achieved by incorporating Pt nanoparticles into MIL-101 (Fe) nanoparticles (Pt@MIL-101) [28] and heterodimer made of upconversion nanoparticles and MOF was demonstrated to be a promising platform for NIR-induced photodynamic therapy for efficient cancer treatment [27]. Core-shell gold

nanorod@MOFs provided a combined photodynamic and photothermal therapy platform [4]. However, the reverse structure of MOF-integrated inorganic nanoparticle (MOF@NP) with multifunction has not been reported yet.

Inspired by the novel properties generated from these NP@MOF hybrids, we developed a facile in-situ growth method to integrate MOF into inorganic nanomaterials. In this method, MOF nanoparticles were used as seed to grow inorganic nanomaterial for potential biochemical applications.  $\text{MnO}_2$  nanosheets have been studied as a novel fluorescence sensing platform for biochemical detection [29-31]. The intrinsic adsorption of dyes and single stranded DNA on  $\text{MnO}_2$  nanosheets induces a significant fluorescence quenching through fluorescence resonance energy transfer (FRET), allowing fluorescence-based target quantification [32-35]. Many studies have proved that Mn ions have cytotoxicity on various cancer cell lines. The exploration of Mn-based photodynamic therapy represents an intriguing avenue to the cancer treatment. Thus, we select  $\text{MnO}_2$  as the inorganic nanomaterial shell to explore the optical property of MOF nanoparticles. We first prepared fluorescent ZIF-8 and hypothesized the  $\text{MnO}_2$  could quench the fluorescence of ZIF-8 after growing on the surface of ZIF-8. Moreover, ZrMOF nanoparticles were synthesized by growing a layer of  $\text{MnO}_2$ . In this case, we hypothesized that  $\text{MnO}_2$  could suppress the photodynamic activity of ZrMOF and a recovery of photodynamic activity can be obtained by decomposing the surface layer of  $\text{MnO}_2$  (Figure 1).

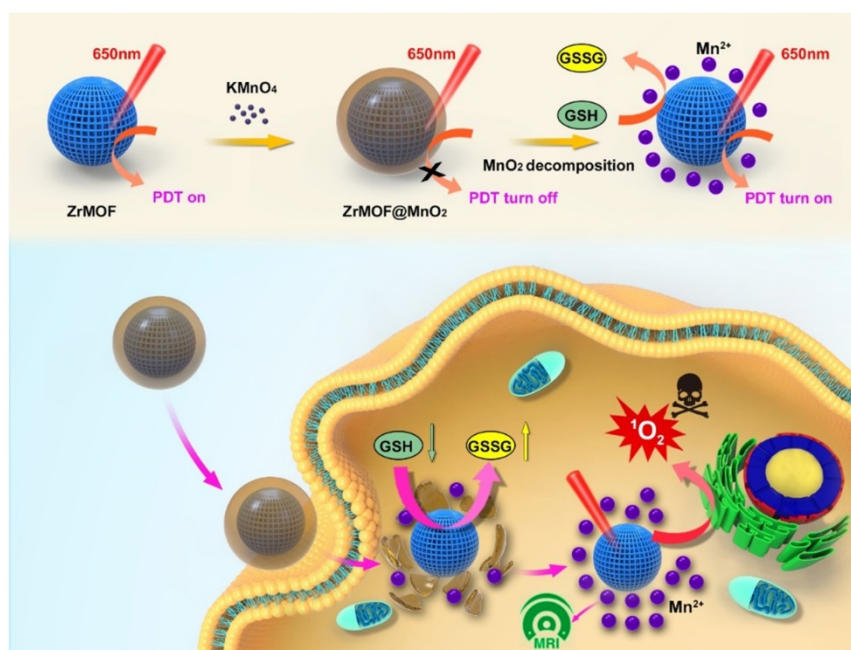


**Figure 1.** Illustration of the in-situ growth method to integrate MOF into inorganic nanomaterials and intracellular GSH-responsive activation of photodynamic activity of ZrMOF@ $\text{MnO}_2$  hybrid nanoparticles for MRI-guided enhanced tumor therapy.

## Results and Discussion

To test our first hypothesis, FITC encapsulated ZIF-8 (ZIF-FITC) [36] was prepared as shown in figure 2A and figure S9. Aqueous  $\text{KMnO}_4$  solution was then introduced to the aqueous ZIF-8 nanoparticle solution with vigorous stirring. A structure with ZIF-FITC nanoparticle core and  $\text{MnO}_2$  nanodot satellites (Figure 2B) was formed quickly upon observing a color change from dark red to brown (Figure 2C). Fluorescence spectroscopy indicated that the fluorescence of the encapsulated FITC was quenched after forming this ZIF-FITC@ $\text{MnO}_2$  hybrid. However, the fluorescence of FITC in the ZIF-8 nanoparticle was recovered (Figure 2D) after introducing GSH to reduce  $\text{MnO}_2$  to Mn ions.

Upon verifying the fluorescence turn-off by  $\text{MnO}_2$  and turn-on by GSH, we further designed a ZrMOF@ $\text{MnO}_2$  hybrid using a similar method as the preparation of ZIF-FITC@ $\text{MnO}_2$  to control the photodynamic activity of porphyrinic MOF. The assembly of porphyrinic photosensitizers to MOF nanoparticles provides many advantages over free photosensitizers in photodynamic therapy. Porphyrinic MOF nanoparticles can accumulate in tumor by the enhanced permeability and retention effect and can then generate cytotoxic singlet oxygen to destroy the tumor. However, as mentioned above, the intracellular GSH can quench the generated

singlet oxygen generated by porphyrinic MOF. This is especially problematic in tumor cells, where the intracellular GSH level is much higher than in normal cells. Therefore, depletion of GSH is a promising way to enhance the photodynamic therapy efficiency.

Based on these features, we grew a thin layer of  $\text{MnO}_2$  nanosheet on the surface of ZrMOF nanoparticles for the one hand to control the photodynamic activity of ZrMOF, for the other hand to deplete the intracellular GSH to enhance the photodynamic therapy efficacy. As shown in figure 3 and figure S1, rather than forming  $\text{MnO}_2$  nanodots, a thin layer of  $\text{MnO}_2$  nanosheet, demonstrated by TEM, HAADF-STEM, and XPS (Figure S2), was formed on the surface of ZrMOF nanoparticles. Dynamic light scattering indicated good colloidal stability of ZrMOF@ $\text{MnO}_2$  (Figure 3G). Compared with ZrMOF nanoparticles, the fluorescence of the ZrMOF@ $\text{MnO}_2$  hybrid was significantly depressed (Figure 4C), although the absorbance did not show a significant change (Figure 4A). The fluorescence depression of porphyrinic MOF is attributed to the FRET between single layer of  $\text{MnO}_2$  and the porphyrinic photosensitizer in ZrMOF. Singlet oxygen generation is the most important index to evaluate the photodynamic activity of the photosensitizers. Singlet oxygen sensor green (SOSG) was used to monitor the generation of singlet oxygen from ZrMOF and ZrMOF@ $\text{MnO}_2$  hybrid nanoparticles. In figure 4D, an increased generation of singlet oxygen was observed when ZrMOF nanoparticles were irradiated with 650 nm laser ( $200 \text{ mW}/\text{cm}^2$ ). In contrast, the singlet oxygen generation from ZrMOF@ $\text{MnO}_2$  was significantly depressed (Figure 4E), indicating that the thin layer of  $\text{MnO}_2$  not only quenches the fluorescence but also depresses the singlet oxygen generation of ZrMOF. However, when GSH was introduced to the ZrMOF@ $\text{MnO}_2$  hybrid nanoparticle solution, the thin layer of  $\text{MnO}_2$  was reduced to  $\text{Mn}^{2+}$  and the GSH was converted to GSSG as the color turned to light brown from dark brown (Figure 4B), resulting in the recovery of singlet oxygen generation (Figure 4F). LC-MS further demonstrated the formation of GSSG from GSH by ZrMOF@ $\text{MnO}_2$  hybrid nanoparticles (Figure 4G). The recovery of fluorescence from the ZrMOF@ $\text{MnO}_2$  hybrid after adding GSH also supports the recovery of singlet oxygen generation (Figure 4C).

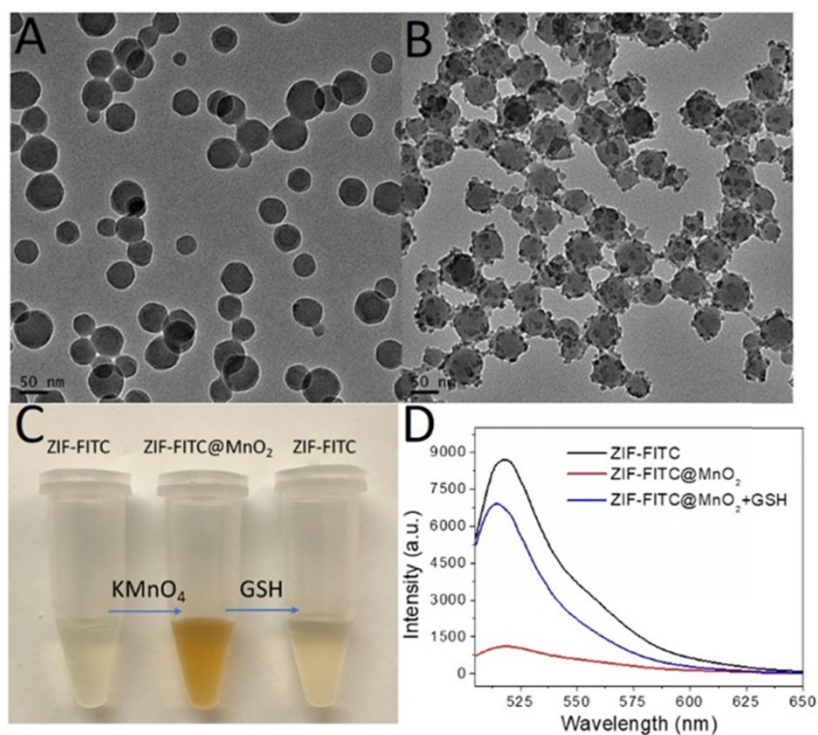


**Figure 2.** ZIF-FITC@ $\text{MnO}_2$  core satellites structure with fluorescence off and on function. (A) TEM of FITC-encapsulated ZIF-8 nanoparticles. (B) TEM of ZIF-FITC@ $\text{MnO}_2$  core satellites nanoparticles. (C) Digital picture of color change after *in situ* growth of  $\text{MnO}_2$  on ZIF-FITC and GSH reduction. (D) Fluorescence turn off by  $\text{MnO}_2$  nanodots and turn on by GSH.

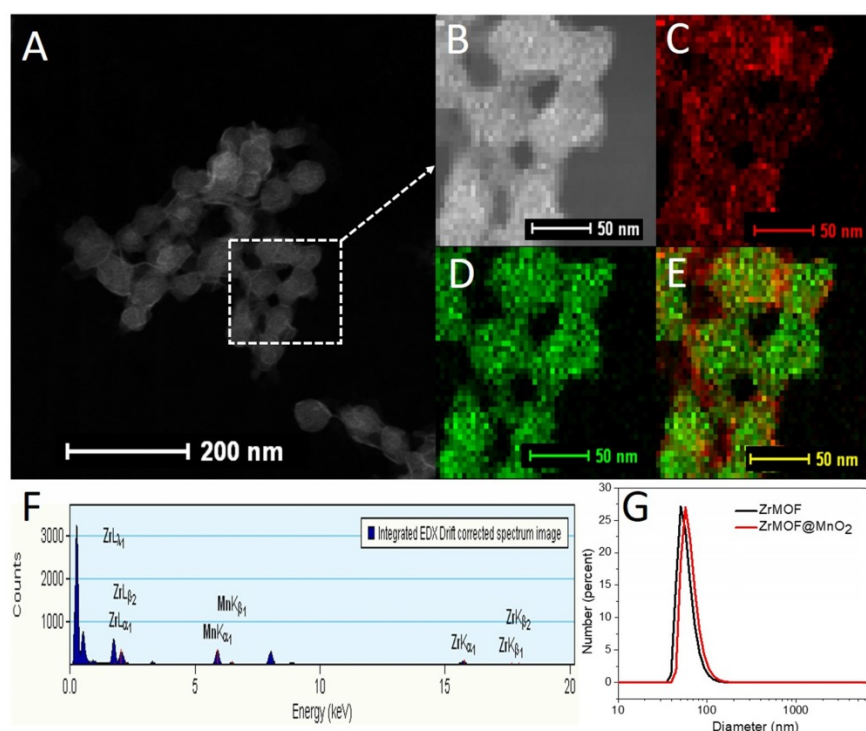


**Figure 3.** (A) HAADF-STEM of ZrMOF@MnO<sub>2</sub>. (B) HAADF-STEM image of area of interest used for element mapping. (C) Mn element map. (D) Zr element map. (E) Mn and Zr composite element map. (F) Sum EDS spectrum of area used for element mapping. (G) Dynamic light scattering of ZrMOF nanoparticles before and after integrating into MnO<sub>2</sub>.

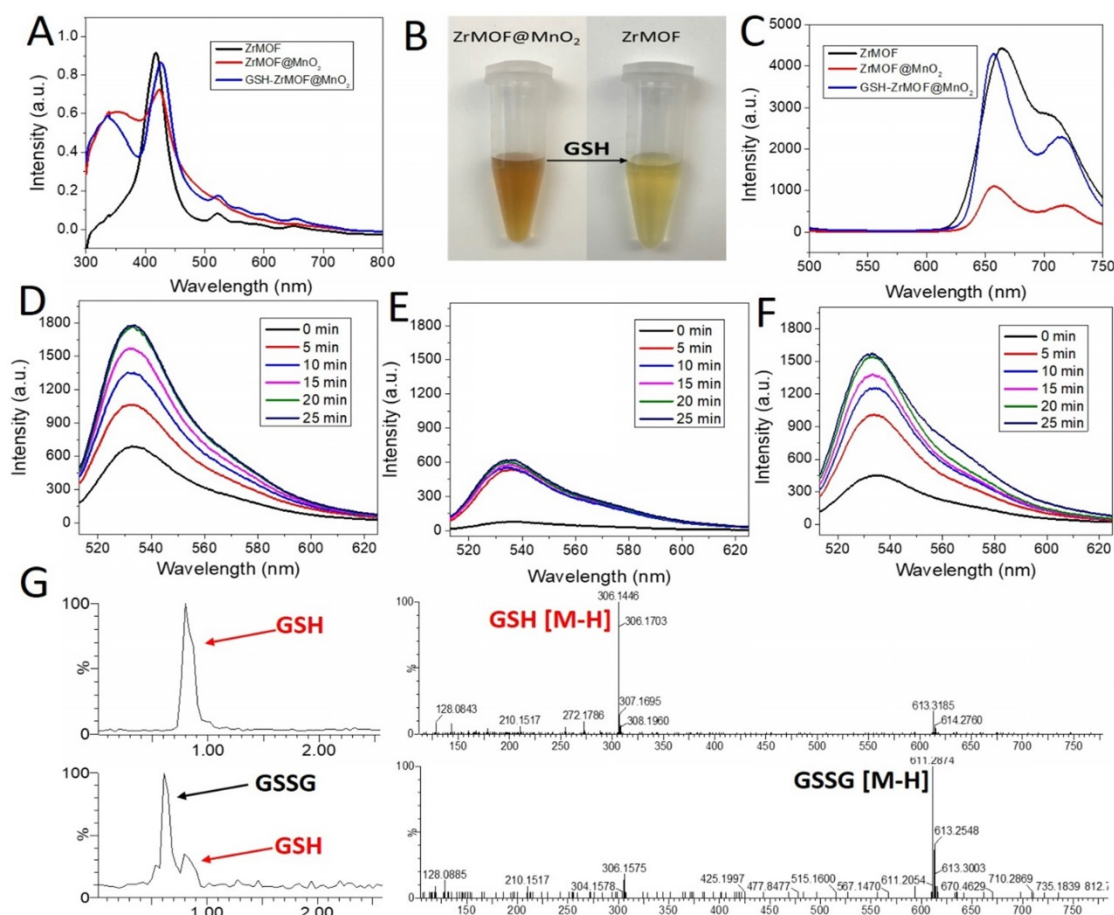


**Figure 4.** (A) UV-vis of ZrMOF, ZrMOF@MnO<sub>2</sub>, and GSH treated ZrMOF@MnO<sub>2</sub>. (B) Digital picture of GSH responsive ZrMOF@MnO<sub>2</sub>. (C) Fluorescence of ZrMOF, ZrMOF@MnO<sub>2</sub>, and GSH treated ZrMOF@MnO<sub>2</sub>. (D) Singlet oxygen generation of ZrMOF. (E) Singlet oxygen generation of ZrMOF@MnO<sub>2</sub>. (F) Singlet oxygen generation of GSH treated ZrMOF@MnO<sub>2</sub>. To measure the singlet oxygen generation, nanoparticles were irradiated with 650 nm laser (200 mW/cm<sup>2</sup>). (G) LC-MS of GSH and GSSG from GSH oxidized by ZrMOF@MnO<sub>2</sub> hybrid nanoparticles.

Having demonstrated that the GSH can decompose the  $\text{MnO}_2$  nanosheet to turn on the photodynamic activity of  $\text{ZrMOF@MnO}_2$  hybrid, we further studied how the GSH level affects the singlet oxygen generation of  $\text{ZrMOF}$  and  $\text{ZrMOF@MnO}_2$  hybrid nanoparticles by treating them with different concentrations of GSH. SOSG probe was first added to the MOF nanoparticle solution. Background from SOSG was measured before laser irradiation (black). After 15 min laser irradiation, generated singlet oxygen was measured (red). Subsequently, different concentrations of GSH were added. Singlet oxygen was measured again immediately after adding GSH (blue). After applying a second 15 min laser irradiation, newly generated singlet oxygen was measured (pink). Significant quenching of singlet oxygen was observed when the concentration of GSH was increased to 0.25 mM and 0.75 mM (Figure 5 top). Furthermore, very few new singlet oxygens were generated even when a second 15 min laser irradiation was applied. The same singlet oxygen monitoring protocol was applied to  $\text{ZrMOF@MnO}_2$  hybrid nanoparticles (Figure 5 bottom). Compared with  $\text{ZrMOF}$  nanoparticles, much less singlet oxygen was generated from  $\text{ZrMOF@MnO}_2$  after 15 min laser irradiation before adding GSH due to the suppressing of photodynamic activity from  $\text{MnO}_2$  nanosheet (red). Upon adding GSH, an increasing number of

generated singlet oxygens were quenched as the concentration of GSH increased after the first (15 min) laser irradiation (blue). For example, when the concentration of GSH increased to 0.75 mM, almost all generated singlet oxygens were quenched by GSH, confirming the strong quenching ability of GSH to singlet oxygen. However, the newly generated singlet oxygen was significantly increased when a second 15 min laser irradiation was applied to  $\text{ZrMOF@MnO}_2$  after adding GSH (pink). This is because an increasing amount of  $\text{MnO}_2$  on the surface of  $\text{ZrMOF}$  nanoparticles was reduced to  $\text{Mn}^{2+}$  by GSH as the concentration of GSH increased from 0.05 mM to 0.1 mM and 0.25 mM. The elimination of  $\text{MnO}_2$  from  $\text{ZrMOF@MnO}_2$  led to the recovery of singlet oxygen generation. However, the generation of new singlet oxygen was depressed again when the concentration of GSH increased to 0.75 mM, because excess GSH were left to quench the newly generated singlet oxygen even though all  $\text{MnO}_2$  nanosheets of  $\text{ZrMOF@MnO}_2$  were reduced. The overall GSH effect on the generation of singlet oxygen of  $\text{ZrMOF}$  and  $\text{ZrMOF@MnO}_2$  under the irradiation of 650 nm laser was summarized in figure 6A. This in vitro balance study of  $\text{MnO}_2$  and GSH on the generation of singlet oxygen provides us insight to obtain enhanced photodynamic therapy. The stoichiometry ratio of  $\text{MnO}_2$  and GSH reaction was further determined to be 1 to 2 by a standard curve, as shown in figure S3.

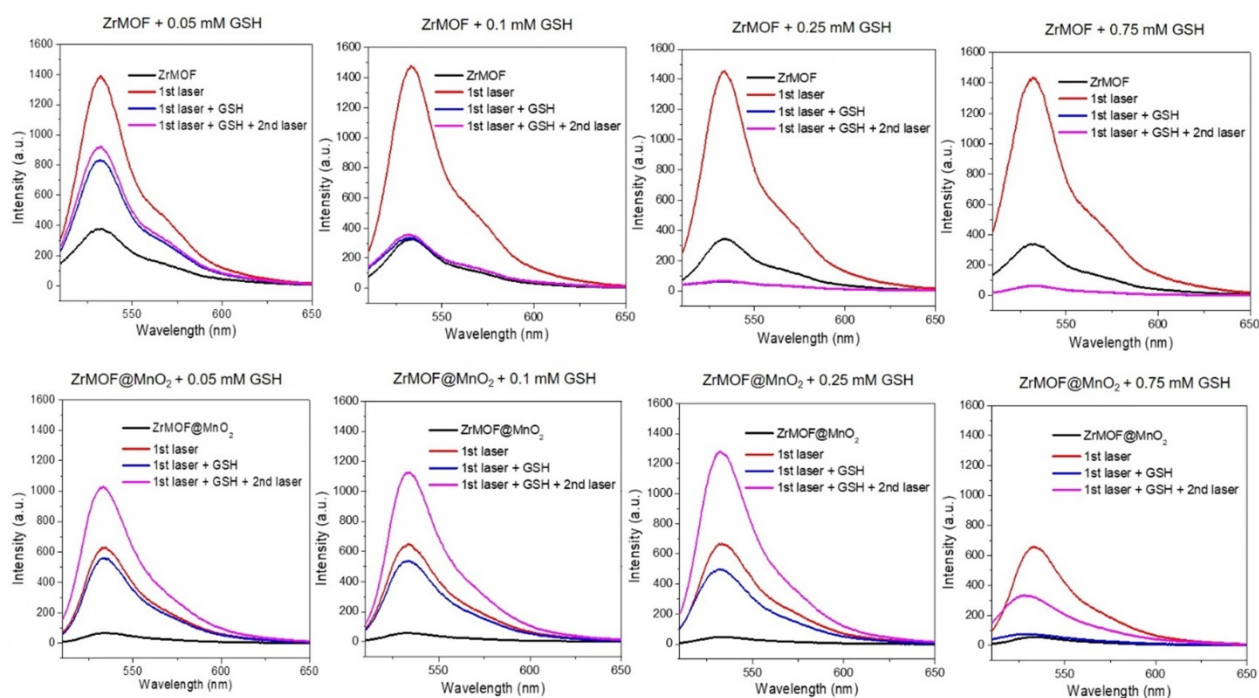


**Figure 5.** Singlet oxygen generation of  $\text{ZrMOF}$  (top) and  $\text{ZrMOF@MnO}_2$  (bottom) with different concentration of GSH. Black: background of singlet oxygen after adding SOSG; red: singlet oxygen generated after 15 min laser irradiation; blue: singlet oxygen generation after adding GSH; pink: generated singlet oxygen after a second 15 min laser irradiation.

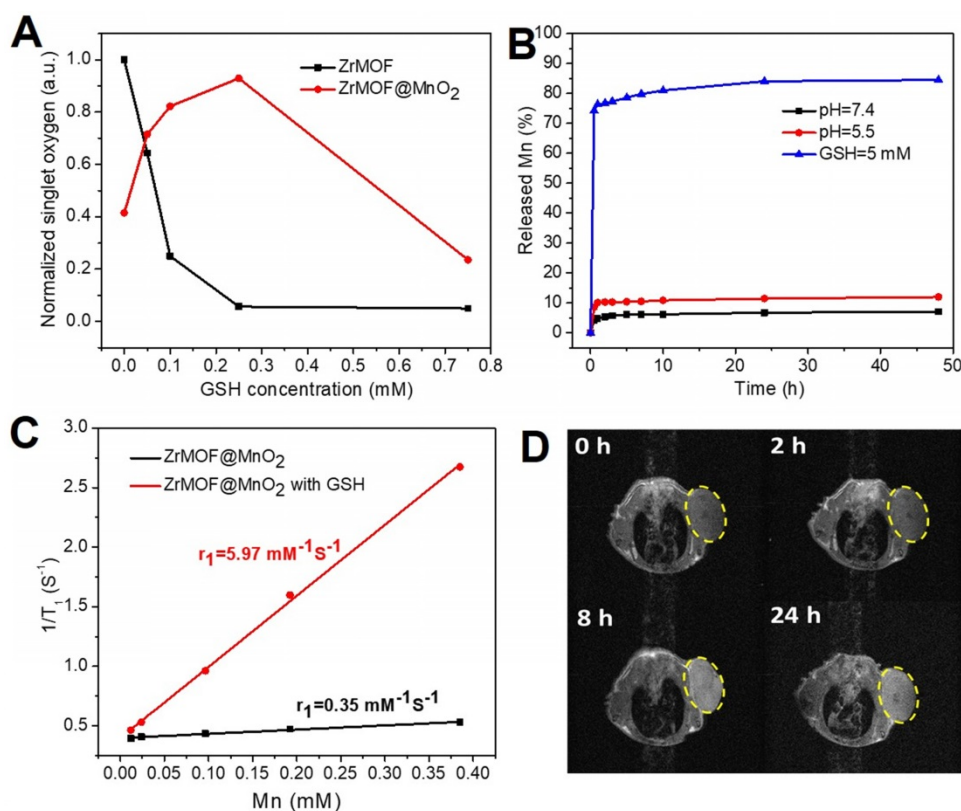


**Figure 6.** (A) The summary of GSH effect on the generation of singlet oxygen of ZrMOF and ZrMOF@MnO<sub>2</sub> under irradiation of 650 nm laser (200 mW/cm<sup>2</sup>). (B) The release behavior of Mn from ZrMOF@MnO<sub>2</sub> under different conditions. (C) The  $r_1$  value of ZrMOF@MnO<sub>2</sub> hybrid nanoparticles with and without GSH. (D)  $T_1$ -weighted images of mice at different times after intravenous injection with PEGylated ZrMOF@MnO<sub>2</sub> hybrid nanoparticles.

To evaluate the photodynamic therapy efficiency of ZrMOF@MnO<sub>2</sub> hybrid nanoparticles, we next conducted MTT assay with ZrMOF@MnO<sub>2</sub> using ZrMOF nanoparticles as control. As shown in figure 7A, ZrMOF@MnO<sub>2</sub> displayed higher cytotoxicity ability compared to ZrMOF under same laser irradiation. In addition, the flow cytometry of cell apoptosis and stained live/dead cell also demonstrated a significantly enhanced photodynamic therapy from ZrMOF@MnO<sub>2</sub> hybrid nanoparticles compared to ZrMOF nanoparticles with the same laser irradiation (Figure S4 and S5). Therefore, the depletion of GSH by MnO<sub>2</sub> can maintain a high level of singlet oxygen generated by ZrMOF, thus improving the cell apoptosis efficiency.

The reduction of MnO<sub>2</sub> by GSH not only depletes GSH to enhance the photodynamic therapy efficiency but also offers us an opportunity to take advantage of the reduction product, Mn<sup>2+</sup>, for magnetic resonance imaging-guided photodynamic therapy. We first studied the release behavior of Mn in vitro using ICP by treating ZrMOF@MnO<sub>2</sub> with sodium acetate (pH=5.5) and GSH (5mM) which are similar with the tumor microenvironment. As shown in figure 6B, a negligible release of Mn (7%) was observed after 48 hours when pH=7.4. Although MnO<sub>2</sub> can be decomposed by acid, pH=5.5 is not strong enough to

quickly decompose all MnO<sub>2</sub> shell on the surface of ZrMOF nanoparticles. Only about 12% of Mn was released after 48 hours when pH=5.5. However, MnO<sub>2</sub> is very sensitive to GSH. About 75% of Mn was released in 1 hour when GSH=5 mM. After 24 hours, the Mn release reached 84% which is almost the maximal level (figure 6B). Thus, GSH plays a major role to decompose MnO<sub>2</sub>.  $T_1$  relaxivity were compared with and without treatment of GSH. A much higher longitudinal relaxivity  $r_1$  was obtained when MnO<sub>2</sub> shell of ZrMOF@MnO<sub>2</sub> were reduced to Mn<sup>2+</sup> in figure 6C, indicating that a GSH-stimulative activation of  $T_1$  contrast can be developed for tumor imaging-guided therapy. To test the potential of ZrMOF@MnO<sub>2</sub> hybrid as an MRI contrast agent, PEGylated ZrMOF@MnO<sub>2</sub> hybrid nanoparticles were intravenously given to mice with U87MG tumor. Figure 6D showed a significant  $T_1$  contrast improvement at the 8th hour after injection from the time dependent  $T_1$ -weighted images of mice, indicating the tumor accumulation of ZrMOF@MnO<sub>2</sub> hybrid nanoparticles and the reduction of MnO<sub>2</sub> to Mn<sup>2+</sup> by GSH. Considering both the Mn release behavior and  $T_1$  contrast information, the laser irradiation for in vivo photodynamic therapy was conducted at the 24th hour after intravenous injection.

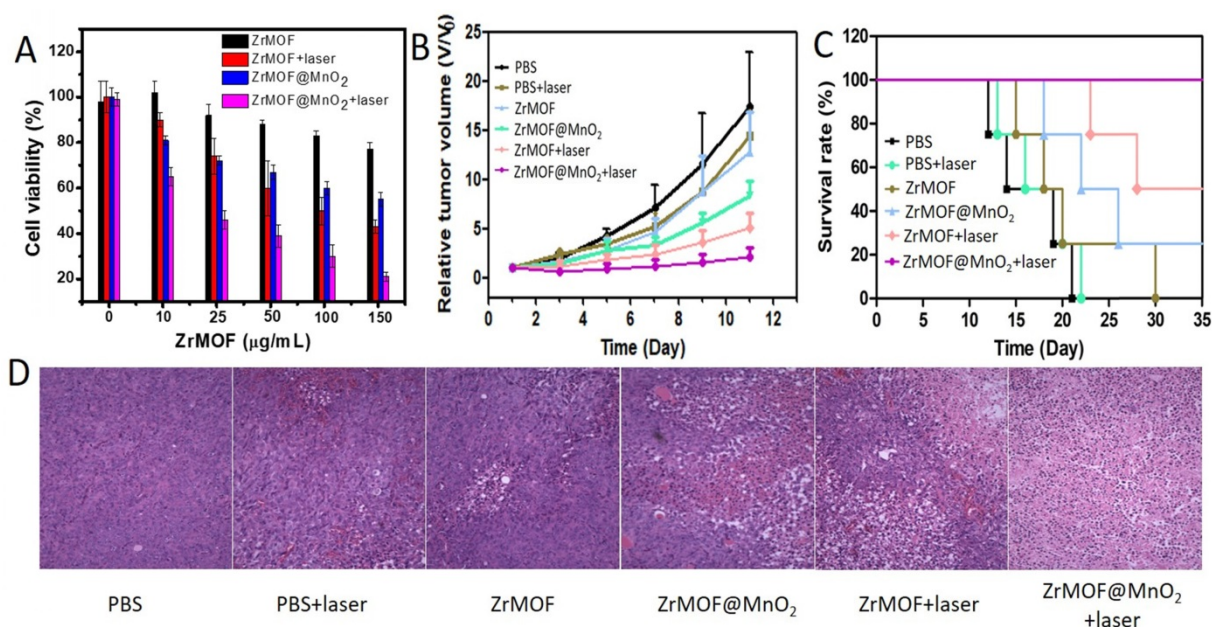


**Figure 7.** (A) Cell viability of U87MG cells with different treatments. (B) The curves of tumor growth after various treatments. (C) Survival rate of mice with U87MG tumor after various treatments. (D) The images of H&E stained tumor sections after various treatments.

Encouraged by the enhanced in vitro photodynamic therapy efficacy of ZrMOF@MnO<sub>2</sub> hybrid nanoparticles and the magnetic resonance imaging-guided therapy information, we further investigated its photodynamic therapy using mice with U87MG tumor. The mice were intravenously given two doses of PEGylated ZrMOF and ZrMOF@MnO<sub>2</sub> nanoparticles every four days for a total of two times. The tumor was irradiated by 650 nm laser at 24th hour following each injection for 15 min at 200 mWcm<sup>-2</sup>. As shown in figure 7B, the tumors of mice grew quickly when treated with PBS or PBS + laser. However, the tumors of mice treated with ZrMOF@MnO<sub>2</sub> hybrid nanoparticles showed significant tumor eradication after laser irradiation. In contrast, ZrMOF-treated mice showed limited tumor inhibition with laser irradiation. The tumor volumes of mice after treatment are presented in figure S6. Furthermore, the mice treated with ZrMOF@MnO<sub>2</sub> hybrid nanoparticles and laser irradiation achieved longer survival times and higher survival rates than the control groups (Figure 7C). This remarkable tumor inhibition is attributed to the intracellular balance of GSH and MnO<sub>2</sub> and the photodynamic activity of ZrMOF nanoparticles accumulated in tumor. After photodynamic therapy, major organs and tumors were obtained for histological analysis. The haematoxylin and eosin (H&E) stained images of tumors from different groups of mice are shown in figure S7. No obvious pathological changes of major organs were observed (Figure 7D). Despite the enhanced photodynamic therapy efficacy from ZrMOF@MnO<sub>2</sub>, no obvious mice body weight

reduction was observed. These results demonstrated that ZrMOF@MnO<sub>2</sub> hybrid nanoparticles have enhanced photodynamic therapy efficiency owing to the intracellular balance of GSH and MnO<sub>2</sub>.

## Conclusions

In conclusion, we have developed a facile in-situ growth method to grow MnO<sub>2</sub> on the surface of MOF nanoparticle and obtained a core-satellites structure with fluorescence off and on function and a core-shell structure with photodynamic activity off and on function. MnO<sub>2</sub>, as an efficient quencher, not only depressed the fluorescence of dye-contained ZIF-8 but also inhibited the generation of singlet oxygen of porphyrinic ZrMOF. Moreover, we figured out how MnO<sub>2</sub> and GSH affect the singlet oxygen generation and achieved an enhanced photodynamic activity. Although the quenching of generated singlet oxygen by MnO<sub>2</sub> and GSH is harmful to the photodynamic therapy, an enhanced photodynamic therapy was achieved from ZrMOF@MnO<sub>2</sub> hybrid nanoparticles by balancing the MnO<sub>2</sub> and GSH. Overall, these results demonstrate a rational design of core-shell ZrMOF@MnO<sub>2</sub> hybrid to reduce the intracellular GSH and trigger an enhanced photodynamic cancer therapy. This work highlights the impact of inorganic nanomaterial on the MOF properties and provides insight to the rational design of multifunctional MOF-inorganic nanomaterial complexes.

## Methods

**Synthesis of ZIF-8:** In a typical synthesis of 50 nm ZIF-8 nanoparticles, Zn(NO<sub>3</sub>)<sub>2</sub> (150 mg) was

dissolved in 7 mL of methanol. Then, 2-methylimidazole (330 mg) was separately dissolved in 7 mL of methanol, and the resulting solution was injected into the Zn solution with vigorous stirring. After 5 minutes, the mixture turned cloudy. The reaction was stopped and the ZIF-8 nanoparticles were washed with methanol and resuspended in DMF for further use.

**Synthesis of zirconium-based porphyrinic MOF (ZrMOF) nanoparticles:** In a typical synthesis,  $ZrOCl_2$  (30 mg), meso-tetra(4-carboxyphenyl)porphyrin (TCPP) (10 mg) and benzoic acid (270 mg) were dissolved in 10 mL of DMF in a 20 mL vial. The solution was sonicated and incubated in an oil bath at 90°C for 5 h. The resulting product was collected by centrifugation, washed with DMF, and resuspended in DMF for further use.

**In situ growth of  $MnO_2$  nanodots on ZIF-8 nanoparticles:** Typically, ZIF-8 nanoparticles were washed with methanol and finally redispersed in deionized water. Aqueous  $KMnO_4$  solution (2mL, 1mg/mL) was introduced to the aqueous ZIF-8 nanoparticle solution with vigorous stirring at room temperature. After 30 min, the resulting ZIF- $MnO_2$  core-satellites hybrid nanoparticles were washed with water and resuspended in water.

**In situ growth of  $MnO_2$  nanosheet on the surface of porphyrinic ZrMOF nanoparticles:** In a typical synthesis, ZrMOF nanoparticles were first washed with water and resuspended in water. Aqueous  $KMnO_4$  solution (2mL, 1mg/mL) was introduced to the aqueous ZrMOF nanoparticle solution with strong stirring at room temperature. The resulting mixture was incubated for 30 min. Finally the product was washed with water and resuspended in water.

**GSH-activated in vitro and in vivo MRI:** Different concentrations of aqueous ZrMOF@ $MnO_2$  nanoparticles were treated with GSH for 5 min. The resulting solutions were scanned by a MRI system. For the in vivo MRI study, PEGylated ZrMOF@ $MnO_2$  nanoparticles were intravenously injected into U87MG tumor-bearing mice. Magnetic resonance images were acquired at different time.

**In vitro cytotoxicity study:** MTT assay was conducted to investigate photodynamic therapy and cytotoxicity. Typically, U87MG cells were seeded in a 96-well plate at a concentration of 5,000 cells per well and cultured at 37 °C, 5%  $CO_2$  for 24 h. The cells were washed with fresh medium and then corresponding MOF nanoparticles were added. The cells with MOF nanoparticles were incubated at 37 °C, 5%  $CO_2$  for 48 h. Then, 10  $\mu$ L of MTT (5 mg/mL in PBS) was added to the cells and incubated for 4 h. Finally, the medium was replaced with 100  $\mu$ L of DMSO. The absorbance

of each well was measured at 490 nm with a plate reader.

**Confocal microscopy:** The U87MG cells were first seeded in an 8-well Lab-Tek cover-glass slide with a concentration of 25,000 cells per well. MOF nanoparticles were added and incubated with cells for 2 hours at 37 °C, 5%  $CO_2$ . After washing with PBS for three times, Z-Fix solution was added to fix the cells at 37 °C, 5%  $CO_2$  for 20 min. Mounting medium with DAPI was then added to stain for 30 min. Confocal images were obtained from a fluorescence microscope (Zeiss LSM 780).

**Live and dead assay:** Cell live/dead assay was conducted with a staining kit. U87MG cells (25,000) were seeded in an 8-well Lab-Tek cover-glass slide for an overnight incubation. ZrMOF and ZrMOF@ $MnO_2$  nanoparticles were added and incubated with U87MG cells for 5 hours. Subsequently, laser irradiation (650 nm, 0.2 W/cm<sup>2</sup>) was applied for 5 min. The Calcium AM/PI working solutions were added to cells and incubated for 30 min. The cells were then washed with PBS after removing the cell culture media. The slides were finally observed under a fluorescence microscope.

## Abbreviations

MOF: metal-organic framework; ZIF: zeolitic imidazolate framework; GSH: glutathione; FRET: fluorescence resonance energy transfer; TEM: transmission electron microscopy; XRD: X-ray diffraction; DLS: dynamic light scattering; PBS: phosphate buffered saline; SOSG: Singlet oxygen sensor green; H&E: hematoxylin and eosin.

## Supplementary Material

The supplementary material includes the characterization data of XPS, TEM, Flow cytometry, Confocal imaging, and XRD used in this study. <http://www.thno.org/v09p2791s1.pdf>

## Acknowledgements

This work supported by intramural research program of the National Institute of Biomedical Imaging and Bioengineering (NIBIB), National Institutes of Health (NIH), the intramural research program of Faculty of Health Science, and the Start-up Research Grant (SRG2018-00130-FHS) at the University of Macau.

## Author Contributions

Y.L., Y.D. and X.C. conceived the idea and designed the experiments. Y.L., C.G., L.L., Y.L., Z.Y., Z.W., G.Y., S.W., W.F., L.H., and G.N. were primarily responsible for the data collection and analysis. Z.Z. and Z.S. performed the in vitro and in vivo MRI. Y.M.

performed LC-MS. Y.L., Y.D., and X.C. analyzed the data and co-wrote the manuscript. All authors discussed the results and commented on the manuscript.

## Competing Interests

The authors have declared that no competing interest exists.

## References

- Huang Z. A review of progress in clinical photodynamic therapy. *Technol Cancer Res Treat.* 2005; 4: 283-93.
- Juarranz Á, Jaén P, Sanz-Rodríguez F, Cuevas J, González S. Photodynamic therapy of cancer. Basic principles and applications. *Clin Transl Oncol.* 2008; 10: 148-54.
- Lismont M, Dreesen L, Wuttke S. Metal-Organic Framework Nanoparticles in Photodynamic Therapy: Current Status and Perspectives. *Adv Funct Mater.* 2017; 27: 1606314.
- Zeng JY, Zhang MK, Peng MY, Gong D, Zhang XZ. Porphyrinic Metal-Organic Frameworks Coated Gold Nanorods as a Versatile Nanoplatform for Combined Photodynamic/Photothermal/Chemotherapy of Tumor. *Adv Funct Mater.* 2018; 28: 1705451.
- Huang P, Lin J, Wang S, Zhou Z, Li Z, Wang Z, et al. Photosensitizer-conjugated silica-coated gold nanoclusters for fluorescence imaging-guided photodynamic therapy. *Biomaterials.* 2013; 34: 4643-54.
- Park J, Jiang Q, Feng D, Mao L, Zhou H-C. Size-controlled synthesis of porphyrinic metal-organic framework and functionalization for targeted photodynamic therapy. *J Am Chem Soc.* 2016; 138: 3518-25.
- Yuan Q, Wu Y, Wang J, Lu D, Zhao Z, Liu T, et al. Targeted Bioimaging and Photodynamic Therapy Nanoplatform Using an Aptamer-Guided G-Quadruplex DNA Carrier and Near-Infrared Light. *Angew Chem Int Ed Engl.* 2013; 125: 14215-9.
- Lin J, Wang S, Huang P, Wang Z, Chen S, Niu G, et al. Photosensitizer-loaded gold vesicles with strong plasmonic coupling effect for imaging-guided photothermal/photodynamic therapy. *ACS Nano.* 2013; 7: 5320-9.
- Yoon M, Srirambalaji R, Kim K. Homochiral metal-organic frameworks for asymmetric heterogeneous catalysis. *Chem Rev.* 2011; 112: 1196-231.
- Furukawa H, Cordova KE, O'Keeffe M, Yaghi OM. The chemistry and applications of metal-organic frameworks. *Science.* 2013; 341: 1230444.
- Feng D, Gu ZY, Li JR, Jiang HL, Wei Z, Zhou HC. Zirconium-metalloporphyrin PCN-222: mesoporous metal-organic frameworks with ultrahigh stability as biomimetic catalysts. *Angew Chem Int Ed Engl.* 2012; 51: 10307-10.
- Horcajada P, Gref R, Baati T, Allan PK, Maurin G, Couvreur P, et al. Metal-organic frameworks in biomedicine. *Chem Rev.* 2011; 112: 1232-68.
- Liu D, Huxford RC, Lin W. Phosphorescent nanoscale coordination polymers as contrast agents for optical imaging. *Angew Chem Int Ed Engl.* 2011; 50: 3696-700.
- He C, Liu D, Lin W. Nanomedicine applications of hybrid nanomaterials built from metal-ligand coordination bonds: nanoscale metal-organic frameworks and nanoscale coordination polymers. *Chem Rev.* 2015; 115: 11079-108.
- Chen Y, Li P, Modica JA, Drout RJ, Farha OK. Acid-Resistant Mesoporous Metal-Organic Framework toward Oral Insulin Delivery: Protein Encapsulation, Protection, and Release. *J Am Chem Soc.* 2018; 140: 5678-81.
- Horcajada P, Chalati T, Serre C, Gillet B, Sebrie C, Baati T, et al. Porous metal-organic-framework nanoscale carriers as a potential platform for drug delivery and imaging. *Nat Mater.* 2010; 9: 172.
- Zheng H, Zhang Y, Liu L, Wan W, Guo P, Nyström AM, et al. One-pot synthesis of metal-organic frameworks with encapsulated target molecules and their applications for controlled drug delivery. *J Am Chem Soc.* 2016; 138: 962-8.
- Chen W-H, Yu X, Ceconello A, Sohn YS, Nechushtai R, Willner I. Stimuli-responsive nucleic acid-functionalized metal-organic framework nanoparticles using pH- and metal-ion-dependent DNAszymes as locks. *Chem Sci.* 2017; 8: 5769-80.
- Liu Y, Hou W, Xia L, Cui C, Wan S, Jiang Y, et al. ZrMOF nanoparticles as quenchers to conjugate DNA aptamers for target-induced bioimaging and photodynamic therapy. *Chem Sci.* 2018; 9: 7505-9.
- Fan H, Yan G, Zhao Z, Hu X, Zhang W, Liu H, et al. A smart photosensitizer-manganese dioxide nanosystem for enhanced photodynamic therapy by reducing glutathione levels in cancer cells. *Angew Chem Int Ed Engl.* 2016; 55: 5477-82.
- Zhang X, Wu FG, Liu P, Gu N, Chen Z. Enhanced fluorescence of gold nanoclusters composed of HAuCl<sub>4</sub> and histidine by glutathione: glutathione detection and selective cancer cell imaging. *Small.* 2014; 10: 5170-7.
- Zhang W, Lu J, Gao X, Li P, Zhang W, Ma Y, et al. Enhanced Photodynamic Therapy by Reduced Levels of Intracellular Glutathione Obtained by Employing a Nano-MOF with CuII as the Active Center. *Angew Chem Int Ed Engl.* 2018; 130: 4985-90.
- Lin LS, Song J, Song L, Ke K, Liu Y, Zhou Z, et al. Simultaneous Fenton-like Ion Delivery and Glutathione Depletion by MnO<sub>2</sub>-Based Nanoagent to Enhance Chemodynamic Therapy. *Angew Chem Int Ed Engl.* 2018; 130: 4996-5000.
- Lu G, Li S, Guo Z, Farha OK, Hauser BG, Qi X, et al. Imparting functionality to a metal-organic framework material by controlled nanoparticle encapsulation. *Nat. Chem.* 2012; 4: 310.
- Zhao X, Feng J, Liu J, Shi W, Yang G, Wang GC, et al. An Efficient, Visible-Light-Driven, Hydrogen Evolution Catalyst NiS/ZnxCd1-xS Nanocrystal Derived from a Metal-Organic Framework. *Angew Chem Int Ed Engl.* 2018; 57: 9790-4.
- He L, Liu Y, Liu J, Xiong Y, Zheng J, Liu Y, et al. Core-Shell Noble-Metal@Metal-Organic-Framework Nanoparticles with Highly Selective Sensing Property. *Angew Chem Int Ed Engl.* 2013; 52: 3741-5.
- Li Y, Di Z, Gao J, Cheng P, Di C, Zhang G, et al. Heterodimers Made of Upconversion Nanoparticles and Metal-Organic Frameworks. *J Am Chem Soc.* 2017; 139: 13804-10.
- Zhao M, Yuan K, Wang Y, Li G, Guo J, Gu L, et al. Metal-organic frameworks as selectivity regulators for hydrogenation reactions. *Nature.* 2016; 539: 76.
- He D, Yang X, He X, Wang K, Yang X, He X, et al. A sensitive turn-on fluorescent probe for intracellular imaging of glutathione using single-layer MnO<sub>2</sub> nanosheet-quenched fluorescent carbon quantum dots. *Chem Commun.* 2015; 51: 14764-7.
- Hu C, Kong XJ, Yu RQ, Chen TT, Chu X. MnO<sub>2</sub> Nanosheet-based Fluorescence Sensing Platform for Sensitive Detection of Endonuclease. *Analytical Sciences.* 2017; 33: 783-8.
- Lin S, Cheng H, Ouyang Q, Wei H. Deciphering the quenching mechanism of 2D MnO<sub>2</sub> nanosheets towards Au nanocluster fluorescence to design effective glutathione biosensors. *Anal Methods.* 2016; 8: 3935-40.
- Zhai W, Wang C, Yu P, Wang Y, Mao L. Single-layer MnO<sub>2</sub> nanosheets suppressed fluorescence of 7-hydroxycoumarin: mechanistic study and application for sensitive sensing of ascorbic acid in vivo. *Anal Chem.* 2014; 86: 12206-13.
- Fan H, Zhao Z, Yan G, Zhang X, Yang C, Meng H, et al. A smart DNAszyme-MnO<sub>2</sub> nanosystem for efficient gene silencing. *Angew Chem Int Ed Engl.* 2015; 127: 4883-7.
- Li J, Li D, Yuan R, Xiang Y. Biodegradable MnO<sub>2</sub> nanosheet-mediated signal amplification in living cells enables sensitive detection of down-regulated intracellular microRNA. *ACS Appl Mater Interfaces.* 2017; 9: 5717-24.
- Deng J, Wang K, Wang M, Yu P, Mao L. Mitochondria targeted nanoscale zeolitic imidazole framework-90 for ATP imaging in live cells. *J Am Chem Soc.* 2017; 139: 5877-82.
- Zhuang J, Kuo C-H, Chou L-Y, Liu D-Y, Weerapana E, Tsung C-K. Optimized metal-organic-framework nanospheres for drug delivery: evaluation of small-molecule encapsulation. *ACS Nano.* 2014; 8: 2812-9.